elektrotechnik und informationstechnik heft 3.2011

OVE Verbands-Verlag

THEMENSCHWERPUNKT

Elektrische Maschinen I

PRAXIS + WISSEN

Überspannnungsschutzgeräte Typ 1 – Funkenstrecke oder Varistor?

INTERVIEW

mit VDir. Ing. Erwin Toplak, Kapsch TrafficCom AG

ZUR HANNOVER MESSE 2011

SpringerWienNewYork

ORIGINALARBEIT

Elektrotechnik & Informationstechnik (2011) 128/3: 86–94. DOI 10.1007/s00502-011-0812-z

Finite element analysis of permanent magnet synchronous machines with fractional slot tooth coil windings

E. Schmidt OVE, M. Sušić

The permanent magnet synchronous machine with an external rotor is the most important device for high performance electrical drive systems in particular for hybrid electric vehicles. The paper discusses finite element analyses of such a machine with concentrated tooth coils in terms of a comparison of both Y- and Δ-connected stator windings. As the evolved electromagnetic torque is one of the most important design parameter, various ratios of tooth width and slot pitch are analyzed with the two connections of the stator winding. On the other hand, the phase voltages are compared between both Y- and Δ-connected stator windings. With an intent of a position sensorless control of the machine, special attention is given to the differential inductances in dependence on the angular rotor position. Finally, the numerically obtained results are compared with measurement results obtained from a prototype machine.

Keywords: permanent magnet synchronous machine; Tooth coil windings; Cogging torque; Finite element analysis

Finite-Elemente-Analysen von Permanentmagnet-Synchronmaschinen mit Bruchloch-Zahnspulenwicklungen.

Permanentmagnet-Synchronmaschinen in Außenläuferbauart zählen zu den wichtigsten Antriebsmaschinen für hochdynamische elektrische Antriebssysteme wie insbesondere in Hybrid-Elektrofahrzeugen. Zwecks Vergleich von Stern- und Dreieckschaltung der Statorwicklung werden Finite-Elemente-Analysen einer solchen Maschine mit einer Statorwicklung aus konzentrierten Zahnspulen beschrieben. Im Hinblick auf das elektromagnetische Drehmoment als der wichtigste Entwurfsparameter werden Geometrievarianten bezüglich verschiedener Verhältnisse von Zahnbreite zur Nutteilung für beide Schaltungen der Statorwicklung untersucht. Als weitere Parameter für den Vergleich der beiden Schaltungsmöglichkeiten der Statorwicklung dienen Strangspannungen und differentielle Induktivitäten. Insbesondere die Abhängigkeit der Induktivitäten von der Rotorwinkellage ist für die Anwendbarkeit einer lagegeberlosen Regelung von großer Bedeutung. Abschließend werden die numerisch ermittelten Ergebnisse mit jenen aus Messungen an einer Prototypmaschine verglichen.

Schlüsselwörter: Permanentmagnet-Synchronmaschine; Zahnspulenwicklung; Rastmoment; Finite-Elemente-Analyse

Received October 11, 2010, accepted February 6, 2011

1. Introduction

The permanent magnet excited synchronous machine (PMSM) with fractional slot stator windings using tooth coil technology provides an increased torque capability due to a more compact construction (*Huth, 2005*; *El-Refaie, Shah, 2008*; *Bianchi, Fornasiero, 2009*; *El-Refaie, 2010*). Thus, the PMSM in particular with an external rotor is the most important device for high performance electrical drive systems such as wheel hub drives of electric driven vehicles. For such an application, there are two main keypoints for the machine design (*Schmidt, 2008*; *Schmidt, Eilenberger, 2009*). First, the torque ripple shows high significance and should be as small as possible. Secondly, a position sensorless control scheme necessary for a robust drive design requires a magnetic saliency even with fast changing load conditions.

The paper discusses finite element analyses of a PMSM with an external rotor and a fractional slot stator winding with tooth coils. Since the voltage of the machine is not fixed with such applications, Y- and Δ-connected stator windings are suitable with respect to their advantages as well as drawbacks. Both connections of the stator winding provide different spectra for magnetic flux and magneto motive force. Thus, the machine parameters such as phase voltages, inductances and electromagnetic torque are significantly influenced by either Y- or Δ-connection of the stator winding. In order to validate the results obtained from the numerical analyses, they are compared with measurement results of a prototype machine.

2. Finite element modelling

Table 1 lists the main data of the investigated PMSM with an external rotor. According to these data, we have the winding data as listed in

Table 1. Main data of the permanent magnet synchronous machine

Number of phases	m	3
Number of poles	$2p$	30
Number of slots	Q	36
Airgap length		2 mm
Inner stator diameter		200 mm
Outer rotor diameter		400 mm
Remanent flux density		1.30 T
Coercive field strength		985.25 kA/m

Schmidt, Erich, Ao. Univ.-Prof. Dipl.-Ing. Dr., Sušić, Marko, Dipl.-Ing., Institute of Energy Systems and Electric Drives, Vienna University of Technology, Gußhausstraße 25-25a, 1040 Vienna, Austria (E-mail: erich.schmidt@tuwien.ac.at)

Table 2. Winding data of the permanent magnet synchronous machine

Number of slots per pole and phase	q	z/n	2/5
Number of base windings	t	p/n	3
Number of slots per base winding	Q^*	Q/t	12
Number of poles per base winding	$2p^*$	$2p/t$	10
Winding pitch	σ	$1/mq$	5/6

Table 2. Consequently, the machine can be equipped with a single-layer fractional slot tooth coil winding of first kind.

As shown in Fig. 1, the smallest necessary section of the entire machine for the finite element model consists of only five poles representing a half of a base winding. To reflect the required periodicity of the magnetic field with the unknown degrees of freedom of the magnetic vector potential, anti-periodic boundary conditions are utilized at the boundaries being five pole pitches apart.

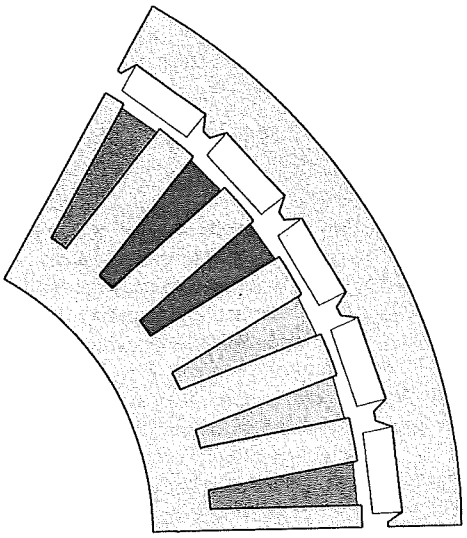

Fig. 1. Cross section of permanent magnet synchronous machine with an external rotor

All analyses utilize fully independent models of rotor and stator denoted as Ω_{rt} and Ω_{st}. The unknown degrees of freedom $\mathbf{U}_m$ of both parts are described with their own matrix equations

$$\left(\mathbf{C}_m \frac{d}{dt} + \mathbf{K}_m\right)\mathbf{U}_m + \mathbf{G}_m = \mathbf{P}_m, \quad m = \{st, rt\}, \tag{1}$$

where $\mathbf{C}_m$, $\mathbf{K}_m$ denote damping and mass matrices, $\mathbf{G}_m$, $\mathbf{P}_m$ represent unknown boundary terms and excitations, respectively.

Both model parts are constructed with an equidistant discretization in circumferential direction along the sliding surface interface Γ_{sl} within the air-gap as shown in Fig. 2 (*Jin, 2002*; *Bastos, Sadowski, 2003*). In dependence on the angular rotor position, these two model parts are coupled together by floating multipoint boundary conditions

$$\mathbf{U}_{rt,e} = \mathbf{E}_k\,\mathbf{U}_{st,e}, \quad \mathbf{G}_{st,e} = -\mathbf{E}_k^T\,\mathbf{G}_{rt,e}, \tag{2}$$

for their exterior unknown degrees of freedom $\mathbf{U}_{m,e}$ along the boundaries Γ_{rt} and Γ_{st} on the sliding surface interface Γ_{sl} (*Bastos, Sadowski, 2003*; *De Gersem et al., 2000, 2003*; *De Gersem, Weiland, 2004*). Consequently, the sliding surface approach completely avoids any remeshing of the air-gap region yielding an identical quality of the numerical results with the analyses of subsequent

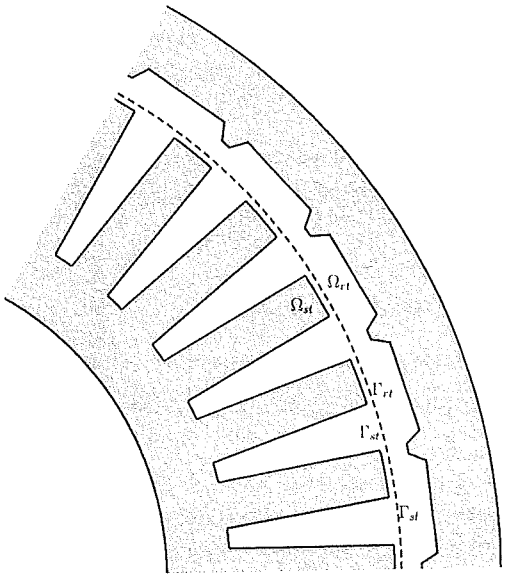

Fig. 2. Domain parts with the sliding surface approach

angular rotor positions (*De Gersem et al., 2003*; *De Gersem, Weiland, 2004*).

3. Space vector calculus

3.1 Two axes inductances

The various analyses are based on the field-oriented control of the PMSM by using stator current and stator flux space vectors. In the dq rotor fixed reference frame (*Park, 1929*; *Kovacs, 1984*), the normalized stator current and stator flux space vectors are given by

$$\underline{i}_{S,dq} = i_S\, e^{j\beta} = i_d + j i_q, \tag{3}$$

$$\underline{\psi}_{S,dq} = \psi_S\, e^{j\vartheta} = \psi_d + j\,\psi_q, \tag{4}$$

where β, ϑ are the stator current angle and the stator flux angle, respectively. The components of the stator linkage flux are usually defined by

$$\psi_d(i_d) = l_{dd}(i_d)\, i_d + \psi_M, \tag{5a}$$

$$\psi_q(i_q) = l_{qq}(i_q)\, i_q, \tag{5b}$$

where l_{dd}, l_{qq} are the direct and quadrature axis inductances and ψ_M denotes the linkage flux of the permanent magnets. On the other hand, very fast changing loads require an introduction of additional cross-coupling inductances l_{dq}, l_{qd} with modified linkage fluxes

$$\psi_d(i_d, i_q) = l_{dd}(i_d, i_q)\, i_d + l_{dq}(i_d, i_q)\, i_q + \psi_M, \tag{6a}$$

$$\psi_q(i_d, i_q) = l_{qd}(i_d, i_q)\, i_d + l_{qq}(i_d, i_q)\, i_q, \tag{6b}$$

3.2 Current injection

In order to inject the stator currents in the $\alpha\beta$ stator fixed reference frame of the finite element model, the stator current and stator flux space vectors are transformed as given by

$$\underline{i}_{S,\alpha\beta} = \underline{i}_{S,dq}\, e^{j\gamma}, \tag{7}$$

$$\underline{\psi}_{S,\alpha\beta} = \underline{\psi}_{S,dq}\, e^{j\gamma}, \tag{8}$$

where γ denotes the electric angular rotor position.

In case of a Y-connected stator winding, any zero sequence stator currents are impossible. Therefore, the stator currents are directly deduced from

$$i_{S1} = \mathrm{Re}\left(\underline{i}_{S,\alpha\beta}\right), \tag{9a}$$

$$i_{S2} = \mathrm{Re}\left(\underline{i}_{S,\alpha\beta}\, e^{\,j2\pi/3}\right), \tag{9b}$$

$$i_{S3} = \mathrm{Re}\left(\underline{i}_{S,\alpha\beta}\, e^{-j4\pi/3}\right). \tag{9c}$$

On the other hand in case of a Δ-connected stator winding, there is an unknown zero sequence current i_0 with all phases. Therefore, the stator currents are now obtained from

$$i_{S1} = i_0 + \mathrm{Re}\left(\underline{i}_{S,\alpha\beta}\right), \tag{10a}$$

$$i_{S2} = i_0 + \mathrm{Re}\left(\underline{i}_{S,\alpha\beta}\, e^{\,j2\pi/3}\right), \tag{10b}$$

$$i_{S3} = i_0 + \mathrm{Re}\left(\underline{i}_{S,\alpha\beta}\, e^{-j4\pi/3}\right). \tag{10c}$$

The unknown zero sequence current i_0 has to be determined iteratively for each angular rotor position with all operating conditions according to the vanishing sum $\psi_{S1} + \psi_{S2} + \psi_{S3} = 0$ of the linkage fluxes of the three phases.

Figure 3 depicts the iteration algorithm of the zero sequence current i_0 which is executed within each analysis. In the first step, the field analysis is carried out without any zero sequence current. In the second step, the field analysis utilizes a zero sequence current of either the negative or positive reference value according to the zero sequence component of the stator linkage flux. Now, the iteration loop based on the Regula Falsi algorithm can be executed. The iteration loop stops when the zero sequence component of the stator linkage flux is less than a predetermined accuracy level.

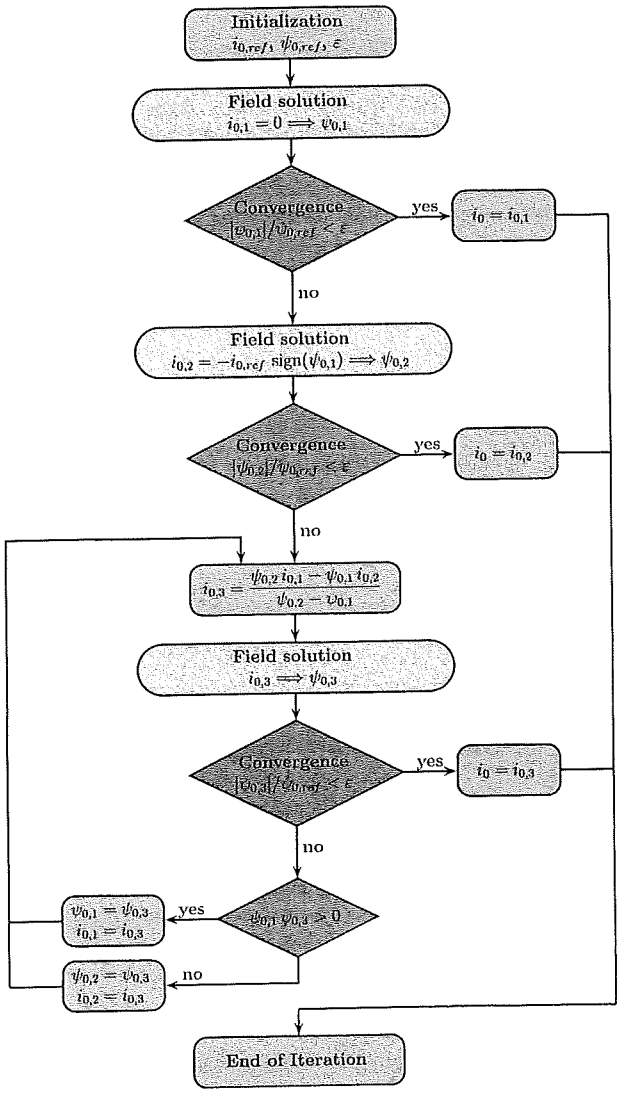

Fig. 3. Iteration algorithm of the zero sequence current

3.3 Complex stator admittance

Neglecting the stator resistance and without the permanent magnets, a constant rotor angular velocity allows for the definition of a complex stator admittance. By using (3)–(8), this admittance reads as

$$\underline{y}_S(\gamma) = \frac{\underline{i}_{S,\alpha\beta}}{\underline{u}_{S,\alpha\beta}} = \frac{1}{2j\omega_S}\left(\frac{1}{l_{dd}} + \frac{1}{l_{qq}}\right) + \frac{1}{2j\omega_S}\left(\frac{1}{l_{qq}} - \frac{1}{l_{dd}}\right)\frac{\underline{u}^{*}_{S,\alpha\beta}}{\underline{u}_{S,\alpha\beta}}\, e^{2j\gamma} \tag{11}$$

without cross-coupling inductances and

$$\underline{y}_S(\gamma) = \frac{\underline{i}_{S,\alpha\beta}}{\underline{u}_{S,\alpha\beta}} = \frac{1}{2j\omega_S}\left(\frac{1}{l_{dd}} + \frac{1}{l_{qq}}\right) + \frac{1}{2j\omega_S}\left(\frac{1}{l_{qq}} - \frac{1}{l_{dd}} + 2j\frac{\sqrt{l_{dq}l_{qd}}}{l_{dd}l_{qq}}\right)\frac{\underline{u}^{*}_{S,\alpha\beta}}{\underline{u}_{S,\alpha\beta}}\, e^{2j\gamma} \tag{12}$$

with cross-coupling inductances.

According to the two-axes approximation and neglecting any saturation, this complex admittance is represented by a circle within the complex plane for any constant stator voltage $\underline{u}_{S,\alpha\beta}$. To obtain a unique information about the angular rotor position γ from the complex stator admittances (11), (12) with all operational states, the difference $l_{dd} - l_{qq}$ of the two-axes inductances should not change the sign. Thus, the magnetic saliency ratio l_{dd}/l_{qq} must be either greater or less than one under all operational conditions.

3.4 Current-torque characteristic

The electromagnetic torque of the PMSM follows as

$$t_i = -\mathrm{Im}\left(\underline{i}^{*}_{S,dq}\, \underline{\psi}_{S,dq}\right) = \psi_d\, i_q - \psi_q\, i_d, \tag{13}$$

consequently (3), (5), (6) yield

$$t_i = \psi_M\, i_q + \left(l_{dd} - l_{qq}\right) i_d\, i_q = \psi_M\, i_S\, \sin\beta + \frac{l_{dd} - l_{qq}}{2}\, i_S^2\, \sin 2\beta \tag{14}$$

without cross-coupling inductances and

$$t_i = \psi_M\, i_q + \left(l_{dd} - l_{qq}\right) i_d\, i_q - \sqrt{l_{dq}l_{qd}}\left(i_d{}^2 - i_q{}^2\right) = \psi_M\, i_S\, \sin\beta + \frac{l_{dd} - l_{qq}}{2}\, i_S^2\, \sin 2\beta - \sqrt{l_{dq}l_{qd}}\, i_S^2\, \cos 2\beta \tag{15}$$

with cross-coupling inductances.

Based on the geometry of the machine as shown in Fig. 1, an inverse-saliency behaviour with $l_{dd} < l_{qq}$ is expected with typical current excitations. Neglecting the cross-coupling inductances, for any given stator current i_S the maximum torque is achieved with a current angle of

$$\cos\beta = -\frac{\psi_M}{4\left(l_{dd} - l_{qq}\right) i_S} - \sqrt{\left(\frac{\psi_M}{4\left(l_{dd} - l_{qq}\right) i_S}\right)^2 + \frac{1}{2}}. \tag{16}$$

Figure 4 shows the typical operational regions of an inverse-saliency PMSM:

- $0 \ldots A$ Operation in the lower speed range, maximum torque from $\cos\beta$ of (16).
- $A \ldots B$ Operation in the field weakening range at current and voltage limits.

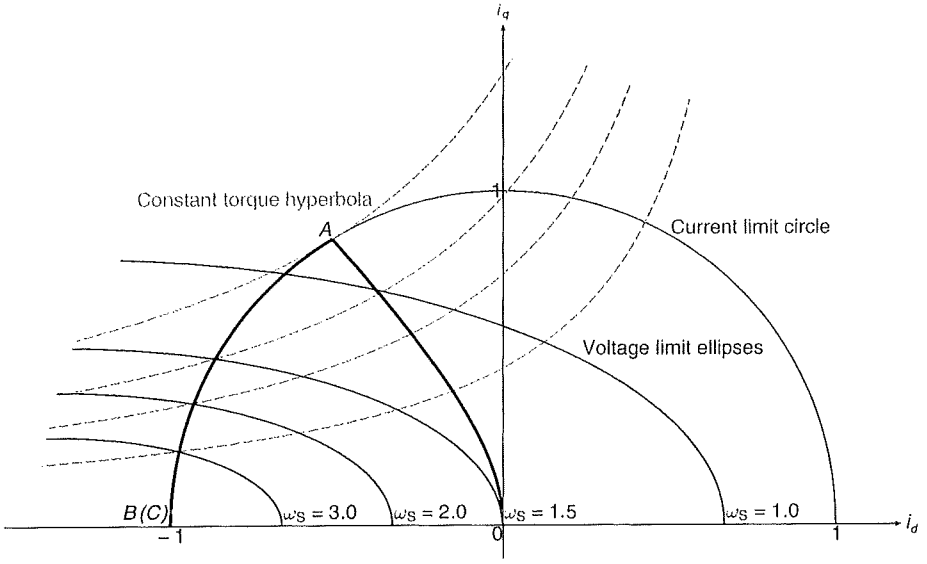

Fig. 4. Operational regions of an inverse-saliency permanent magnet synchronous machine

- $B \ldots C$ Operation in the field weakening range at voltage limit, maximum torque with $\beta_B < \beta < \pi$ when voltage limit ellipses and torque hyperbola are tangential.

Of course, the inverse-saliency PMSM can operate at $\beta = \pi/2$ in the lower speed range. But obviously, the same torque can be produced with smaller stator currents when using the current angles (16) which decreases the power losses and consequently increases the efficiency of the PMSM significantly.

On the other hand, the inverse-saliency PMSM can operate on the current limit in a wide speed range. In case of increased voltage and current limits of the inverter, the machine can generate much higher torque values without demagnetizing the permanent magnets. Therefore, the inverse-saliency PMSM shows an inherent suitability for electrical drives where short overload operational conditions require high torque values.

4. Analysis results

4.1 Comparison with measurements

Figures 5 and 6 depict no-load phase voltages and zero sequence currents of both finite element analysis and measurements for the initial design with the Δ-connected stator winding for the speed of 668 rpm. Obviously, there is a very good agreement between numerical analysis and measurement results.

Additionally, Fig. 7 depicts the average value of the load torque with the initial design in dependence on the quadrature axis current. The numerical results are shown for both Y-connected and Δ-connected stator windings while the measurement results are obtained from the initial design with a Δ-connected stator winding. There is a good agreement with stator currents in the range up to rated current loads but increasing deviations with higher current loads. They arise from stray field portions in the axial direction in particular with the permanent magnets of the rotor.

4.2 No-load voltages

Figures 8 and 9 depict the no-load voltages of one phase with various ratios b_t/τ_s of tooth width and slot pitch and all three phases with the initial design for the speed of 320 rpm for both Y- and Δ-connected stator windings. Accordingly, Tables 3 and 4 list the magnitudes of the significant harmonics in dependence on the ratio b_t/τ_s.

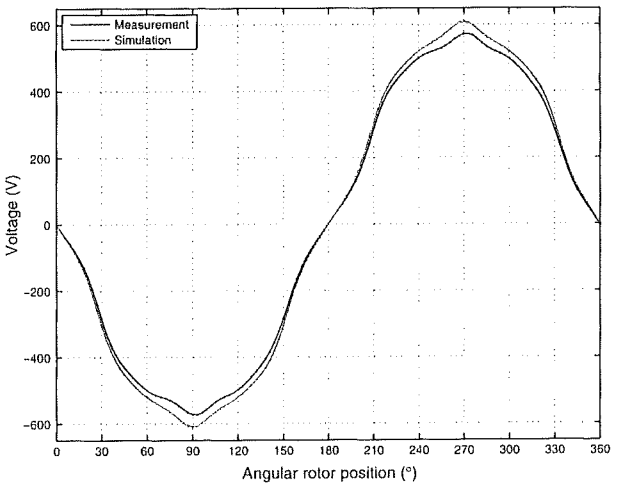

Fig. 5. No-load voltage of the initial design, Δ-connected stator winding, numerical analysis and measurement results

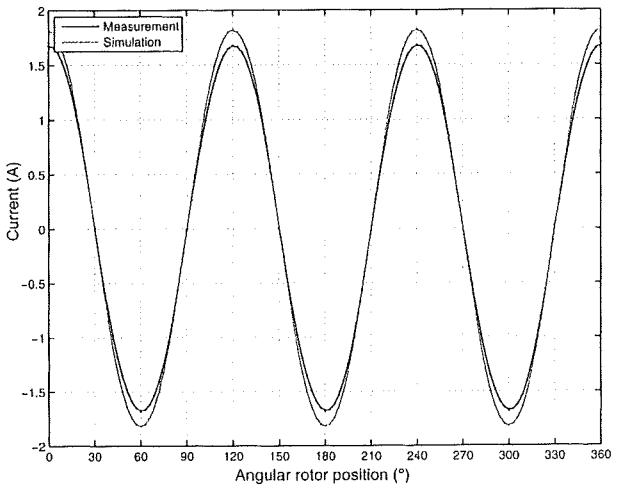

Fig. 6. No-load zero sequence current of the initial design, Δ-connected stator winding, numerical analysis and measurement results

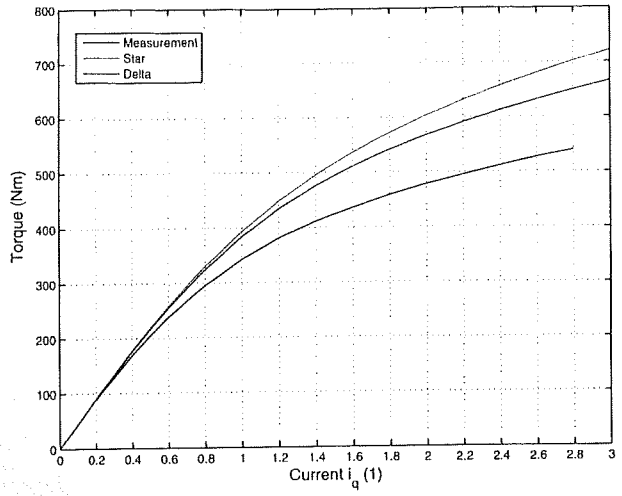

Fig. 7. Load torque of the initial design, Y-connected and Δ-connected stator winding as well as measurement results

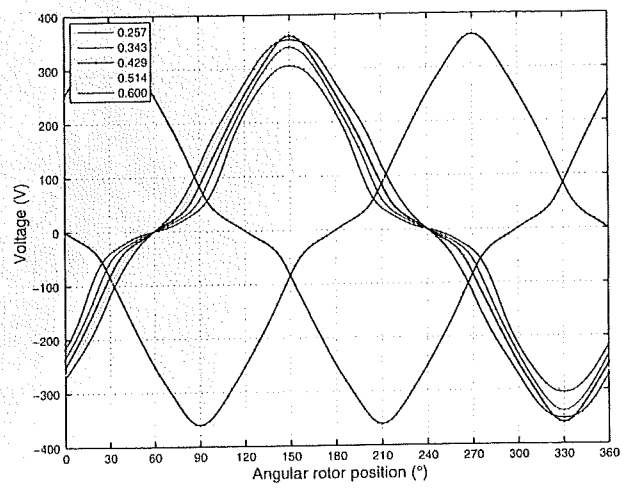

Fig. 8. No-load voltages with various ratios b_t/τ_s of tooth width and slot pitch, Y-connected stator winding

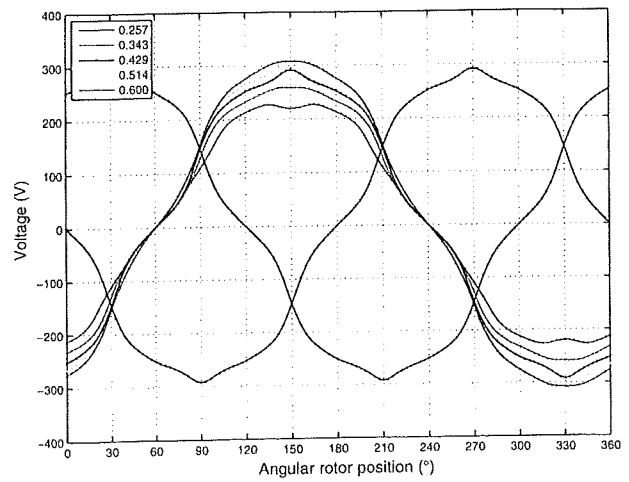

Fig. 9. No-load voltages with various ratios b_t/τ_s of tooth width and slot pitch, Δ-connected stator winding

Table 3. No-load voltage harmonics (magnitudes) with various ratios of tooth width and slot pitch, Y-connected stator winding

	Ratio	Voltage (V)				
	b_t/τ_s	1st order	3rd order	5th order	7th order	9th order
	0.257	239.9	73.0	4.1	6.8	3.0
	0.300	255.9	71.7	4.7	2.6	4.8
	0.343	270.1	69.0	4.4	1.3	4.9
	0.386	282.3	65.3	3.7	4.1	4.3
(ID)	0.429	292.6	61.2	3.3	6.0	3.6
	0.471	301.0	56.7	3.4	7.1	2.7
	0.514	307.9	51.4	3.9	7.4	1.6
	0.557	313.5	45.4	4.6	7.0	0.2
	0.600	317.9	38.5	5.4	6.0	1.4

Table 4. No-load voltage harmonics (magnitudes) with various ratios of tooth width and slot pitch, Δ-connected stator winding

	Ratio	Voltage (V)				
	b_t/τ_s	1st order	3rd order	5th order	7th order	9th order
	0.257	236.3	0.0	14.5	1.6	0.0
	0.300	252.1	0.0	14.6	6.3	0.0
	0.343	266.2	0.0	14.7	10.4	0.0
	0.386	278.5	0.0	14.7	13.3	0.0
(ID)	0.429	288.8	0.0	14.7	14.5	0.0
	0.471	297.4	0.0	14.7	14.4	0.0
	0.514	304.5	0.0	14.9	13.4	0.0
	0.557	310.4	0.0	15.0	11.9	0.0
	0.600	315.3	0.0	14.8	10.0	0.0

In comparison of the Y- and Δ-connected stator windings, the latter generates a smaller fundamental harmonic with all ratios b_t/τ_s. Due to the high level of saturation, the no-load voltages contain a significant third harmonic with all design variations in case of the Y-connected stator winding. On the other hand, there is no third harmonic in case of the Δ-connected stator winding. Moreover, the fifth and seventh harmonics are higher with the Δ-connected stator winding than with the Y-connected stator winding.

4.3 Two axes inductances

The dependence of the magnetic saliency on the angular rotor position with various stator currents in particular in the quadrature axis is one of the most important facts for an implementation of a position sensorless control scheme for the PMSM.

The linkage flux associated with the current carrying regions of the three phases

$$\Psi = \frac{\int_\Omega \mathbf{A} \cdot \mathbf{J}\, d\Omega}{\int_\Gamma \mathbf{J} \cdot \mathbf{n}\, d\gamma} \tag{17}$$

allows for an approximation of the normalized linkage flux

$$\psi(i_0, \Delta i) \approx \psi_0(i_0) + \psi_1(i_0)\,\Delta i \tag{18}$$

yielding the nonlinear differential inductance as

$$l_\psi(i_0) = \psi_1(i_0) = \frac{\psi(i_0, +\Delta i) - \psi(i_0, -\Delta i)}{2\Delta i}. \tag{19}$$

Neglecting the deviations of the inductances with respect to the actual operating point, the differential two-axes inductances l_{dd}, l_{qq} as well as the cross-coupling inductances l_{dq}, l_{qd} can be obtained from

$$\Delta\psi_d(i_d, i_q) \approx l_{dd}(i_d, i_q)\,\Delta i_d + l_{dq}(i_d, i_q)\,\Delta i_q, \qquad (20a)$$

$$\Delta\psi_q(i_d, i_q) \approx l_{qd}(i_d, i_q)\,\Delta i_d + l_{qq}(i_d, i_q)\,\Delta i_q. \qquad (20b)$$

Figures 10 and 11 depict the saliency ratios $l_{dd}(i_d)/l_{qq}(i_q)$ obtained from the differential two-axes inductances averaged along the circumferential direction with various ratios b_t/τ_s for both connections of the stator winding. Obviously, this saliency ratio l_{dd}/l_{qq} in terms of the differential inductances changes the behaviour when the machine operates in a deep field weakening range. This arises from a

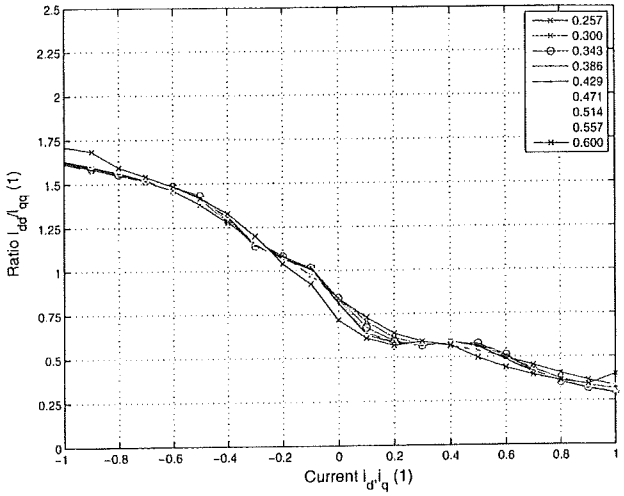

Fig. 10. Ratio $l_{dd}(i_d)/l_{qq}(i_q)$ with various stator tooth widths, Y-connected stator winding

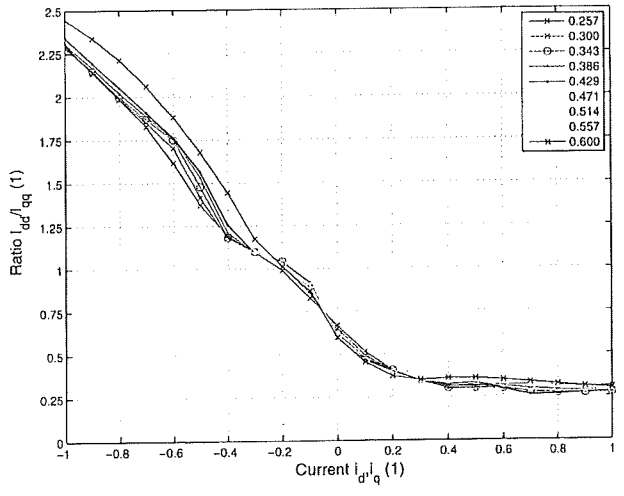

Fig. 11. Ratio $l_{dd}(i_d)/l_{qq}(i_q)$ with various stator tooth widths, Δ-connected stator winding

decreased magnetic saturation in particular with the direct axis. In this high speed range, an accurate information about the angular rotor position can be successfully obtained without any high frequency pulse patterns. Thus, the changing magnetic saliency does not have any further effects on the drive control in the lower speed range.

Finally, Figs. 12, 13 and 14 depict the differential two-axes inductances l_{dd}, l_{qq} and the differential cross-coupling inductances $l_{dq} = l_{qd}$ in dependence on the angular rotor position with various stator currents $i_{s,dq} = i_d$ and $i_{s,dq} = j\,i_q$ for the initial design.

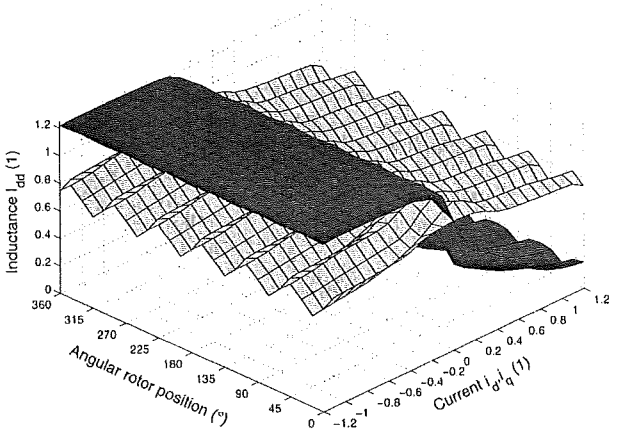

Fig. 12. Inductances $l_{dd}(i_d, 0)$ (dark-coloured), $l_{dd}(0, i_q)$ (light-coloured) of the initial design in dependence on the angular rotor position

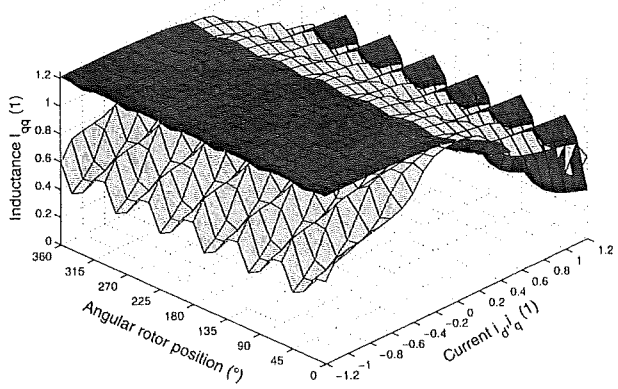

Fig. 13. Inductances $l_{qq}(i_d, 0)$ (dark-coloured), $l_{qq}(0, i_q)$ (light-coloured) of the initial design in dependence on the angular rotor position

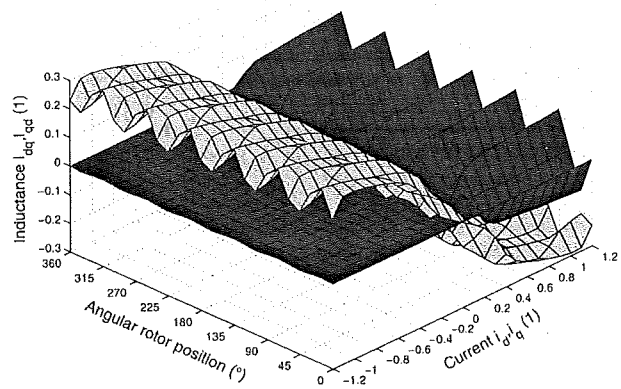

Fig. 14. Inductances $l_{dq}(i_d, 0) = l_{qd}(i_d, 0)$ (dark-coloured), $l_{dq}(0, i_q) = l_{qd}(0, i_q)$ (light-coloured) of the initial design in dependence on the angular rotor position

Both two-axes and cross-coupling inductances are significantly influenced by the stator current excitation and also by the angular rotor position. With the exception of the field weakening range

with stator currents $i_d < 0$ arising mostly in the high speed range, the characteristics of these differential inductances show a dominant higher harmonic component caused by the stator slots. According to the sign of the quadrature current, the angular position of these higher harmonics changes with all distributions. As the effects of the stator slots gain in significance with higher stator currents, positive and negative values of both cross-coupling inductances occur.

Nevertheless, the magnetic saliency ratio l_{dd}/l_{qq} in terms of the differential inductances even with concerning the cross-coupling of the two-axes is preserved to values less than one under all operating conditions with the exception of the field weakening range. As these operational states arise mostly in the high speed range, the position sensorless control based on position dependent differential stator inductances can be successfully applied in the lower speed range.

4.4 Electromagnetic torque

As mentioned above, a cogging torque as small as possible is the most important criterion for a drive system of an electric vehicle.

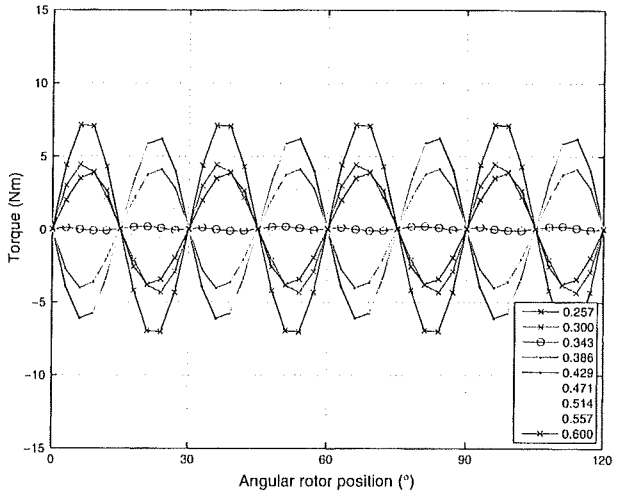

Fig. 15. Cogging torque with various ratios b_t/τ_s of tooth width and slot pitch, Y-connected stator winding

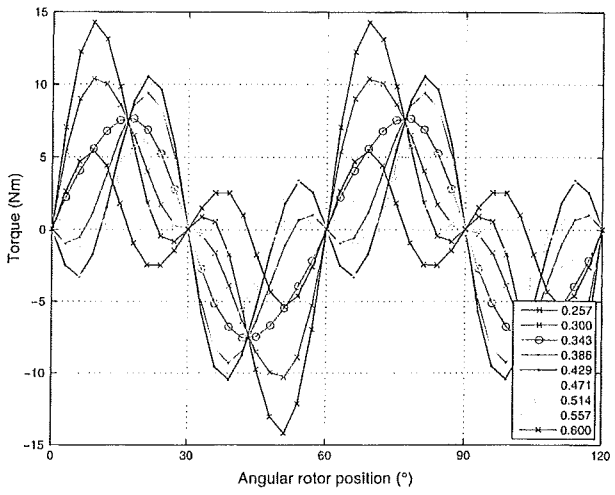

Fig. 16. Cogging torque with various ratios b_t/τ_s of tooth width and slot pitch, Δ-connected stator winding

Figures 15 and 16 as well as Figs. 17 and 18 depict cogging and load torque with various ratios b_t/τ_s of tooth width and slot pitch for both Y- and Δ-connected stator windings, respectively. Accordingly,

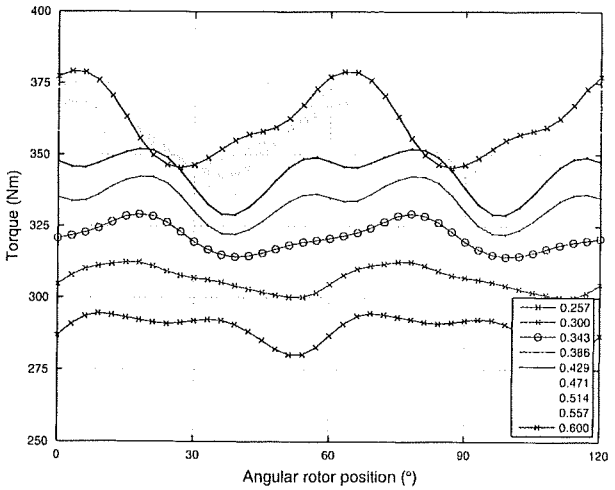

Fig. 17. Load torque with various ratios b_t/τ_s of tooth width and slot pitch, Y-connected stator winding

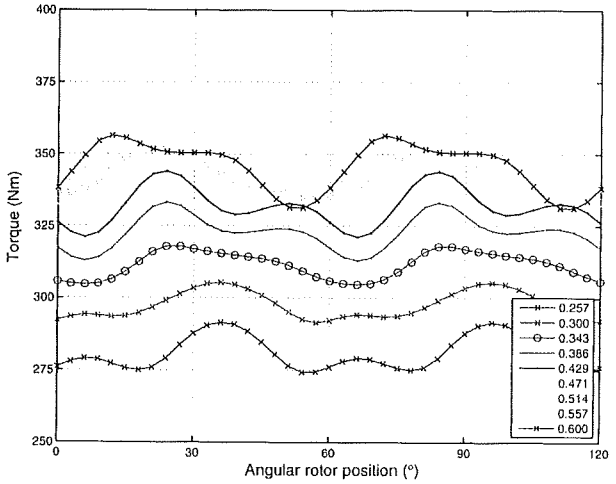

Fig. 18. Load torque with various ratios b_t/τ_s of tooth width and slot pitch, Δ-connected stator winding

Table 5. Load and cogging torque harmonics (magnitudes) with various ratios of tooth width and slot pitch, Y-connected stator winding

	Ratio b_t/τ_s	Average	Load torque (Nm)		Cogging torque (Nm)	
			6th order	12th order	6th order	12th order
	0.257	289.2	5.3	3.7	0.0	7.4
	0.300	306.4	5.6	1.5	0.0	4.3
	0.343	321.1	6.4	2.3	0.0	0.1
	0.386	333.3	7.5	4.9	0.0	4.1
(ID)	0.429	343.2	8.9	5.8	0.0	6.3
	0.471	350.9	10.5	4.3	0.0	5.9
	0.514	356.4	12.2	1.2	0.0	3.2
	0.557	359.8	13.8	2.3	0.0	0.5
	0.600	361.1	15.2	4.7	0.0	3.8

Table 6. Load and cogging torque harmonics (magnitudes) with various ratios of tooth width and slot pitch, Δ-connected stator winding

	Ratio b_t/τ_s	Average	Load torque (Nm)		Cogging torque (Nm)	
			6th order	12th order	6th order	12th order
	0.257	280.9	6.8	4.6	9.9	6.6
	0.300	297.6	6.2	2.0	8.8	3.6
	0.343	311.6	6.1	1.9	7.6	0.6
	0.386	322.9	6.2	5.2	6.5	4.5
(ID)	0.429	331.9	6.5	6.5	5.4	6.6
	0.471	338.7	7.1	5.3	4.4	6.2
	0.514	343.1	8.0	2.3	3.5	3.4
	0.557	345.5	9.0	2.1	2.6	0.6
	0.600	345.8	10.2	5.1	1.8	4.0

Tables 5 and 6 list the magnitudes of the significant harmonics in dependence on the ratio b_t/τ_s.

In comparison of the Y- and Δ-connected stator windings, the first one shows harmonic components of the cogging torque according to the least common multiple of the number of slots and the number of poles as well as multiples,

$$\nu = \frac{g}{p}\,\mathrm{lcm}(Q, 2p) = 12g, \quad g \in \mathcal{N}. \tag{21}$$

On the other hand with the latter one, there are harmonic components of orders $6g$, $g \in \mathcal{N}$, and in particular a noticeable sixth harmonic component in the cogging torque resulting from the zero sequence current in the three phases.

The Δ-connection against the Y-connection generates a higher cogging torque and simultaneously a smaller mean value of the load torque with also a smaller total harmonic distortion in case of an identical stator current injection with all ratios b_t/τ_s.

With both connections, two design variations yield a significantly smaller 12th harmonic component in the cogging torque than the initial design (ID). With respect to a lower saturation level, the higher value of the ratio b_t/τ_s should be preferred.

Finally, Figs. 19 and 20 depict the trajectories for a constant electromagnetic torque with the initial design. In comparison with Fig. 4, the inverse-saliency behaviour with a saliency ratio l_{dd}/l_{qq} of the apparent two-axes inductances slightly less than one is confirmed. On the other hand, the saliency ratio l_{dd}/l_{qq} of the apparent two-axes inductances changes to values slightly greater than one in the very deep field weakening range. As mentioned above, this is caused by a desaturation mainly with the direct axis with these operational conditions.

4.5 Comparison between Y- and Δ-connection

In summary, the Y-connected stator winding, in particular due to the high third harmonic, will generate higher iron losses than the Δ-connected stator winding. On the other hand, the zero sequence current of the Δ-connected stator winding will generate slightly more power losses in the stator windings.

Further, the Δ-connection shows more significant higher harmonic components with the cogging torque and smaller mean values of the load torque with the same stator currents. Nevertheless, the 6th harmonic component is always less for the Δ-connected stator winding than for the Y-connected stator winding. Consequently, the Δ-connection produces a better total harmonic distortion and a smoother load torque along the circumferential direction for the same stator currents.

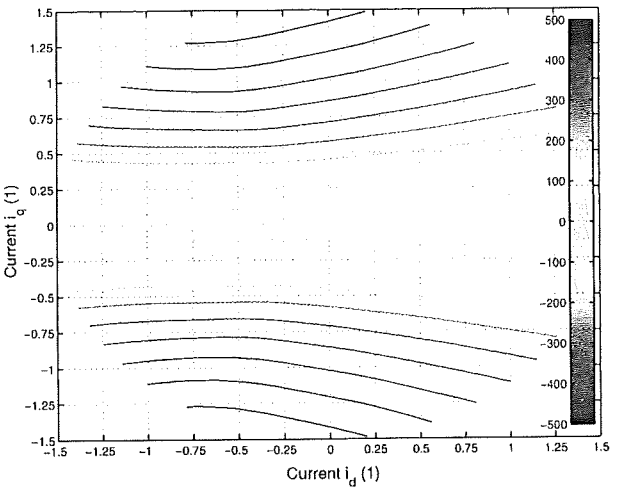

Fig. 19. Constant torque trajectories of the initial design, Y-connected stator winding

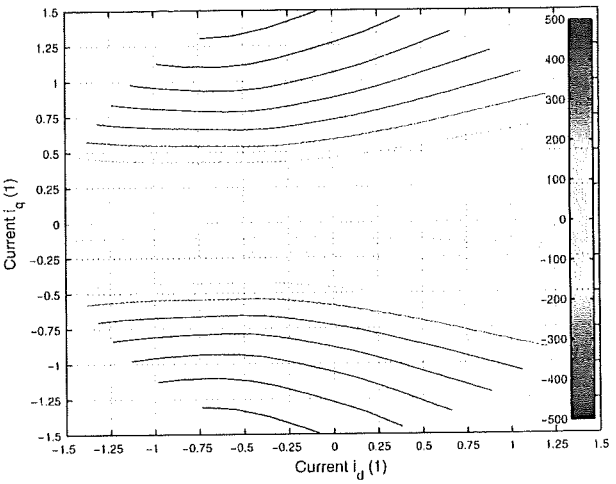

Fig. 20. Constant torque trajectories of the initial design, Δ-connected stator winding

5. Conclusion

The paper discusses parametric finite element analyses of an external rotor PMSM with either a Y- or Δ-connected stator winding. In order to obtain an optimized machine design in terms of the two main keypoints of a small torque ripple and a magnetic saliency ratio necessary for the position sensorless control scheme, geometry variations concerning various ratios of tooth width and slot pitch are carried out. Thereby, no-load voltages, differential inductances and evolved electromagnetic torque in dependence on the angular rotor position are shown in detail.

With all results, both Y- and Δ-connected stator windings are compared against the advantages and drawbacks. On the other hand, the numerically obtained results are successfully compared with the results obtained from measurements of a prototype design of the external rotor PMSM. Consequently, an optimization of the machine design can be carried out in the design stage without a prototype of the machine.

References

Bastos, J. P. A., Sadowski, N. (2003): Electromagnetic modeling by finite element methods. New York, USA: Marcel Dekker Ltd.

Bianchi, N., Fornasiero, E. (2009): Impact of MMF space harmonic on rotor losses in fractional-slot permanent-magnet machines. IEEE Transactions on Energy Conversion, 24 (2): 323–328.

De Gersem, H., Weiland, T. (2004): Harmonic weighting functions at the sliding surface interface of a finite element machine model incorporating angular displacement. IEEE Transactions on Magnetics, 40 (2): 545–548.

De Gersem, H., Mertens, R., Lahaye, D., Vandewalle, S., Hameyer, K. (2000): Solution strategies for transient, field-circuit coupled systems. IEEE Transactions on Magnetics, 36 (4): 1531–1534.

De Gersem, H., Gyselinck, J., Dular, P., Hameyer, K., Weiland, T. (2003): Comparison of sliding surface and moving band techniques in frequency-domain finite element models of rotating machines. Proceedings of the 6th International Workshop on Electric and Magnetic Fields, EMF, Aachen (Germany).

El-Refaie, A. M. (2010): Fractional slot concentrated windings synchronous permanent magnet machines: opportunities and challenges. IEEE Transactions on Industrial Electronics, 57 (1): 107–121.

El-Refaie, A. M., Shah, M. R. (2008): Comparison of induction machine performance with distributed and fractional-slot concentrated windings. IEEE Industry Applications Society Annual Meeting, IAS, Edmonton (AB, Canada).

Huth, G. (2005): Permanent magnet excited AC servo motors in tooth coil technology. IEEE Transactions on Energy Conversion, 20 (2): 300–307.

Jin, J. (2002): The finite element method in electromagnetics. New York, USA: John Wiley & Sons.

Kovacs, P. K. (1984): Transient phenomena in electrical machines. Amsterdam: Elsevier.

Park, R. H. (1929): Two-reaction theory of synchronous machines, generalized method of analysis – Part I. AIEE Transactions, 48 (3): 716–727.

Schmidt, E. (2008): Comparison of different designs of normal and permanent magnet excited reluctance machines. Proceedings of the 9th International Conference on Modeling and Simulation of Electrical Machines, Converters and Systems, ELECTRIMACS, Quebec City (QC, Canada).

Schmidt, E., Eilenberger, A. (2009): Calculation of position dependent inductances of a permanent magnet synchronous machine with an external rotor by using voltage driven finite element analyses. IEEE Transactions on Magnetics, 45 (3): 1788–1791.

Authors

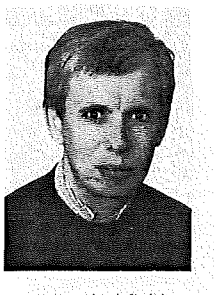

Erich Schmidt
was born in Vienna, Austria, in 1959. He received his M.Sc. and Ph.D. degrees in Electrical Engineering from the Vienna University of Technology, Austria, in 1985 and 1993, respectively. Currently, he is an Associate Professor of Electrical Machines at the Institute of Energy Systems and Electric Drives at the Vienna University of Technology. His research and teaching activities are on numerical field computation techniques and design optimization of electrical machines and transformers. He has authored more than 100 technical publications mainly in the fields of electrical machines and numerical field calculation.

Marko Sušić
was born in Klagenfurt, Austria, in 1980. He received his B.Sc. and M.Sc. degrees in Electrical Engineering from the Vienna University of Technology, Austria, in 2008 and 2010, respectively. Currently, he is with the scientific staff at the Institute of Energy Systems and Electric Drives at the Vienna University of Technology and works toward his Ph.D. thesis on design and control of permanent magnet synchronous machines.